Journal of Alloys and Compounds 691 (2017) 130–137

Contents lists available at ScienceDirect

Journal of Alloys and Compounds

journal homepage: http://www.elsevier.com/locate/jalcom

Structural and magnetic influence of yttrium-for-iron substitution in cobalt ferrite

Isaac Haïk Dunn [a], Silvia E. Jacobo [b], Paula G. Bercoff [a, *]

[a] Facultad de Matemática, Astronomía, Física y Computación (FaMAF), Universidad Nacional de Córdoba, IFEG, CONICET, Medina Allende s/n, Ciudad Universitaria, Córdoba, Argentina
[b] DiQuiMMAI, Facultad de Ingeniería, Universidad de Buenos Aires, INTECIN, CONICET, Av. Paseo Colón 850, Buenos Aires, Argentina

ARTICLE INFO

Article history:
Received 21 June 2016
Received in revised form
2 August 2016
Accepted 22 August 2016
Available online 24 August 2016

Keywords:
Ceramics
Oxide materials
Crystal structure and symmetry
X-ray diffraction
Raman spectroscopy
Magnetic measurements

ABSTRACT

Yttrium-substituted cobalt ferrites of nominal composition $CoY_xFe_{1.98-x}O_4$, x = 0; 0.1; 0.2; 0.3, were prepared using the sol-gel combustion method. A slight iron deficiency in the formulation was designed in order to improve yttrium solubility in the spinel structure. The inclusion of Y in the lattice reached 10% cationic substitution. XRD Rietveld analysis and Raman spectra confirm that yttrium enters the lattice in octahedral sites, increasing the inversion parameter of cobalt ferrite. Mössbauer results confirm the cation distribution obtained with Rietveld refinements. Saturation magnetization and Curie temperature decrease with iron substitution, confirming the B site occupancy of Y ions. Yttrium inclusion promotes a cation distribution which modifies the Raman spectra. A model is proposed to explain the observed vibrational modes.

1. Introduction

Cobalt ferrite ($CoFe_2O_4$) is a well-known and widely used ferrimagnetic hard material because of its wide range of applications in environmental science, recording media, magnetic sensors and catalytic materials, among others [1]. Its crystal system is face centered cubic while its crystal structure is mixed spinel, whose corresponding space group is O^7_h (Fd-3m). Its unit cell consists of 56 atoms where 32 of them are oxygen anions and the remaining 24 atoms are metallic cations divided such that 8 of them occupy tetrahedral (A) sites and 16 occupy octahedral (B) sites. The cation distribution is generally represented as $(Co^{2+}_{\delta}\ Fe^{3+}_{1-\delta})_A[Co^{2+}_{1-\delta}Fe^{3+}_{1+\delta}]_B O^{2-}_4$, where δ is the inversion parameter (which is 1 for a normal spinel and 0 for an inverse spinel structure), and is extremely important because it determines the electromagnetic properties of the material. For most ferrites, δ depends upon the method of preparation, while cation distribution is related to the thermal treatment [2]. Previous studies reported an inversion parameter δ~0.2–0.3 for cobalt ferrite [3].

Over the last years, several authors [4–9] have studied the effects of the substitution of Fe^{3+} by rare earth (RE) cations such as Y^{3+}, Gd^{3+} or La^{3+} in the magnetic and structural properties of cobalt ferrite. Few works have reported the synthesis of single phase RE-substituted spinel ferrites, although relatively low concentrations of the dopants were explored (cationic substitution <7%). The presence of secondary phases is attributed mainly to the large size of the RE cation, which finds it difficult to fit in either tetrahedral or octahedral sites. The electric, magnetic and microwave absorption properties of ferrites can be controlled by substitution with RE ions, and changes in these properties are related to the segregation of secondary phases in grain boundaries, so it is important to control RE solubility in ferrites [10,11].

To our knowledge there is only one study, albeit non exhaustive, of yttrium-substituted cobalt ferrite with a nominal Y cationic substitution of 7% which is reported as single phase [6]. It is therefore of interest to further deepen the study of yttrium solubility in cobalt ferrite.

In earlier works, we achieved an enhancement of Nd solubility in the crystalline structure of Sr hexaferrites, obtaining single phase materials by proposing an iron deficient formulation [12–14]. Taking these previous results into account, in this work we intend to enhance Y substitution up to 10% in Co ferrite, by proposing a slight iron deficiency in the formulation. A thorough structural

---

* Corresponding author.
E-mail address: bercoff@famaf.unc.edu.ar (P.G. Bercoff).

http://dx.doi.org/10.1016/j.jallcom.2016.08.223

analysis is performed using different characterization techniques.

2. Experimental details

2.1. Samples preparation

All the samples were prepared by the self-combustion method, as described elsewhere [15]. For synthesizing $CoFe_2O_4$, different proportions of iron nitrates and cobalt oxalates were weighed according to the required stoichiometric proportion and diluted in water (considering that $[Fe(III)]+[Co(II)] = 1$ M). A 3 M citric acid solution (50 ml) was added to each metal solution (50 ml) and heated at 40 °C for approximately 30 min with continuous stirring. The final mixture was slowly evaporated until a highly viscous gel was formed. The resulting gel was heated at $T < 200$ °C; when it ignited in a self-propagated process. The final residue was calcined at 800 °C for 2 h.

Yttrium nitrates, previously dissolved in 3 M citric acid solutions, were used for the preparation of the Y-doped samples ($CoY_xFe_{1.98-x}O_4$, $x = 0.1; 0.2; 0.3$). A slight deficiency in iron content was considered (1 at.%) for all the substitutions.

The obtained samples were labeled Y0, Y1, Y2 and Y3, being the number related to the yttrium content, x. The samples labels and nominal compositions are shown in Table 1.

2.2. Characterization methods

In order to determine the actual composition of the prepared powders, Inductively Coupled Plasma Atomic Emission Spectroscopy (ICP-AES) was performed. An Ar plasma Spectro Modula Flame was used. The detection limits for Fe, Co and Y were 0.25 ppm, 1 ppm and 0.25 ppm, respectively.

X-ray diffraction (XRD) powder diffractograms were measured with a Philips PW 3860 diffractometer, in the 2θ range 20–110, with a step size of 0.02, for 8 s per step. A Sigma Zeiss Field Emission scanning electron microscope with an Oxford EDS detector (LAMARX facilities) was used to characterize the morphology and elemental composition of the samples.

A ^{57}Co source (Rh matrix) was used to record Mössbauer spectra in constant acceleration mode, at room temperature. Powder samples (65 mg) were measured in a round acrylic sample holder of 20 mm diameter. The measured isomer shifts (IS) are referred to α-Fe. The Normos/site Program was used for fitting the measured spectra.

Raman spectra were measured at room temperature with a laser Raman spectrophotometer (Confocal Horiba Jobin-Yvon LabRam HR). The excitation wavelength and laser power were 632.8 nm and 2.8 ± 0.2 mW, respectively. Spectra were acquired by averaging from three different spots in each sample in order to improve statistical uncertainties.

The magnetic properties were measured with a Lakeshore 7300 vibrating sample magnetometer, at room temperature, with a maximum applied field of 14.5 kOe. The Curie temperature T_C was determined using a differential calorimeter SDT Q600 (TA Instruments) in N_2 atmosphere and under magnetic field, with a heating rate of 10 °C/min. TG curves of weight vs temperature were used to determine T_C as the maximum of the derivative d(weight)/dT.

Table 1
Nominal and ICP compositions of the prepared samples.

Sample label	Y content	Nominal composition	ICP composition
Y0	0	$CoFe_2O_4$	$CoFe_2O_4$
Y1	0.1	$CoFe_{1.88}\,Y_{0.10}O_4$	$CoFe_{1.79}\,Y_{0.08}O_4$
Y2	0.2	$CoFe_{1.78}\,Y_{0.20}O_4$	$CoFe_{1.70}\,Y_{0.18}O_4$
Y3	0.3	$CoFe_{1.68}\,Y_{0.30}O_4$	$CoFe_{1.69}\,Y_{0.27}O_4$

3. Results and discussion

3.1. Composition and crystalline structure

The actual composition of the samples, determined by ICP, is listed in Table 1. It is interesting to remark that ICP are very close to nominal compositions. In this work, all the structural analyses will be performed considering the ICP values.

Fig. 1 shows the diffractograms of all the prepared samples where the main spinel reflections are indexed.

All the samples have the cubic spinel structure, matching the JCPDS-PDF 22-1086 standard. The XRD peaks indicate the presence of a single phase up to Y3, where the evidence of a very small amount of a secondary phase, indexed as yttrium orthoferrite $YFeO_3$, can be noticed as a shoulder near the (311) reflection peak (Fig. 1).

All the XRD patterns were refined using the Rietveld method [16] with the aid of the Fullprof Suite software, based on a refinement using the Fd-3m space group. The Pseudo-Voight function was used to define the peak profile and a nine-coefficient polynomial was used to fit the background. The initial model and atomic coordinates were taken from the literature. A typical X-ray diffraction pattern, along with Rietveld refined data for sample Y2 have been depicted in Fig. 2. For all the samples, the profiles of observed and calculated data perfectly match to each other and all the experimental peaks are allowed Bragg 2θ positions for the Fd-3m space group. Oxygen positions and other atomic fractional positions were taken as fixed parameters, while lattice constants, isothermal parameters, cation occupancies, scale factors and shape parameters were set as free parameters for the fitting.

The relevant parameters from the refinements, together with the reliability factors (R_{exp}, R_{wp}) and the goodness of fit (GOF) are listed in Table 2. The GOF values obtained for all the refinements (close to 1) indicate the fits are quite reliable.

The cation vacancy in B sites and the inversion parameter δ were calculated using the cationic distribution obtained with the Rietveld refinements, and are listed in Table 2, together with the cell parameters. The inversion parameter δ which is ~0.2 for Y0,

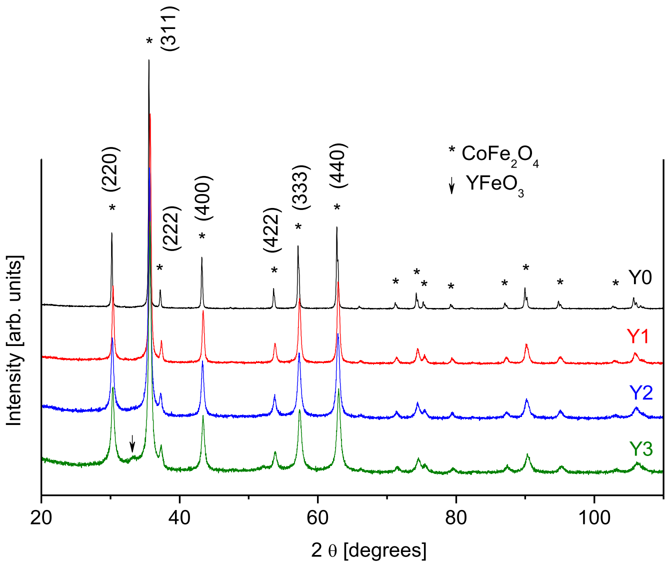

Fig. 1. X ray diffractograms of samples Y0 to Y3.

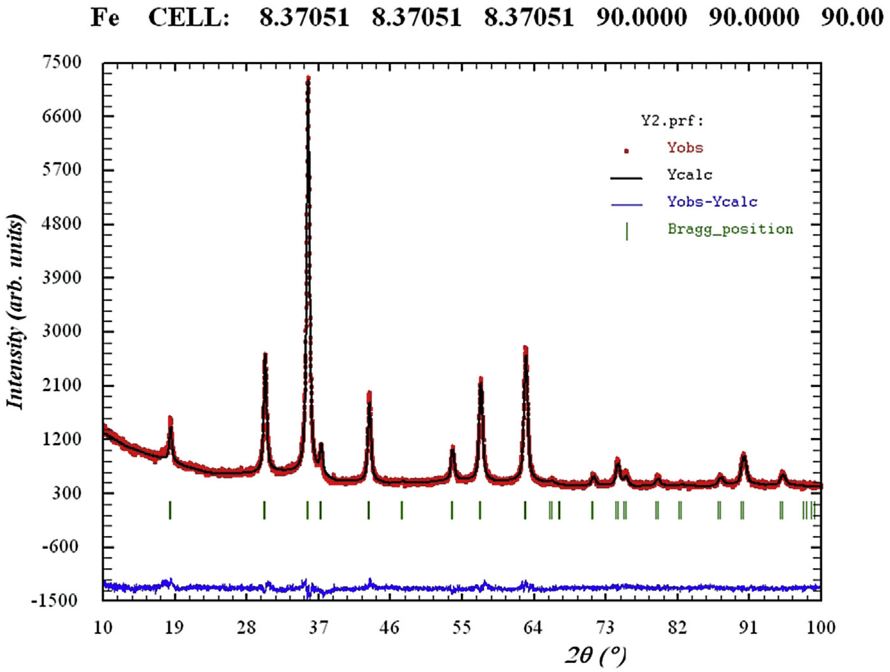

Fig. 2. Rietveld refined XRD pattern of sample Y2. The circles represent experimental data and the solid line is the calculated pattern. The bottom line shows the difference between experimental and refined data. The marked 2θ positions are the allowed Bragg reflections for the spinel structure.

Table 2
Cation distribution in A and B sites, inversion parameter (δ), cell parameter (a) and Rietveld refinement figures of merit.

	Co (A)	Fe (A)	Co (B)	Fe (B)	Y (B)	Cation vacancy in B sites	Inversion parameter δ	$YFeO_3$	a (Å)	R_{exp}	R_{wp}	GOF
Y0	0.198	0.802	0.802	1.198	0	0	0.198	–	8.37176(4)	4.09	4.33	1.12
Y1	0.333	0.667	0.667	1.123	0.080	6.5%	0.333	–	8.37051(6)	4.04	4.82	1.43
Y2	0.264	0.736	0.736	0.964	0.180	6%	0.264	–	8.35744(6)	3.87	4.42	1.30
Y3	0.224	0.776	0.776	0.893	0.257	3.7%	0.224	1.2%	8.35022(6)	3.78	4.57	1.46

changes with Y inclusion.

A systematic decrease in cell parameters is observed with Y inclusion, despite the large size of Y^{3+} (1.04 Å) compared to that of Fe^{3+} (0.69 Å). Other researchers [5,7,8,17] have also reported similar results when doping a spinel with RE cations. This slight decrease in a (0.3%) with increasing Y substitution can be explained by considering the cation distribution and the cation sizes. Co^{2+} (0.79 Å) and Fe^{3+} occupy both A and B sites. When the large yttrium ions replace the smaller Fe^{3+} in B sites, lattice strains and local structural disorder appear. In order to compensate for this strain, the larger cation Co^{2+} moves from B to A sites, producing a slight lattice contraction. It is unlikely that this effect is related to cation vacancies in B sites (Table 2) as it decreases from Y1 to Y3.

Mössbauer spectra recorded at room temperature are shown in Fig. 3. The spectra were fitted to two sextets related to the Zeeman interaction between the hyperfine magnetic field and the nuclear magnetic moment, and a doublet due to the existence of a small fraction of superparamagnetic particles of low crystallinity. The subspectra sextets are assigned to iron ions located in the tetrahedral (Fe-A) and octahedral (Fe-B) sites. The fitting of sample Y3 was done adding a new sextet to account for the contribution of the orthoferrite phase. The fitted results for all the samples are shown in Table 3. The isomer shift (IS) and hyperfine magnetic field (B_{hf}) values are typical for cobalt ferrites [18]. The difference in IS values obtained for the tetrahedral and the octahedral sites are ascribed to the great covalence of iron ion. The relative areas of A and B sites, R_A and R_B respectively, depend upon Y substitution so the distribution of Fe ions in the lattice can be calculated from the ratio $R_A/R_B = f_A/f_B$ (x/(2-x)), where the ratio of recoilless fraction between octahedral and tetrahedral sites at 300 K is $f_B/f_A = 0.94$ [18].

For our samples, the iron distribution was calculated using the expression $F_i = n_{Fe}\, R_A/(R_B + R_A)$, being n_{Fe} the amount of Fe atoms per formula unit considering the vacancies confirmed by ICP results. In every case, the amount of Fe atoms corresponding to the SP doublet was considered. In Y3, the secondary phase was also taken into account. The values for F_A and F_B are listed in Table 3 and are in good agreement with the cation distribution obtained by Rietveld refinements (Table 2).

3.2. Morphology of the powders

Fig. 4 a–d show SEM images of the powders and Fig. 4 e displays the particle size distributions calculated from the images. For determining the particles sizes, several images were processed with the software ImageJ.

The images reveal that all the samples are composed by faceted nanoparticles, with a narrow size distribution. Yttrium inclusion drastically reduces grain size D_m from 85 nm in Y0 to 46 nm in Y1, while keeping a mean size around this value for the other Y contents (Table 4). The average crystallite sizes, D_{Sch}, were estimated with the Scherrer formula using XRD results and are also presented in Table 4. Both D_m and D_{Sch} have a similar tendency, which can be related to the lattice disorder after yttrium inclusion (as previously discussed) as well as the induced strains that inhibit the grain

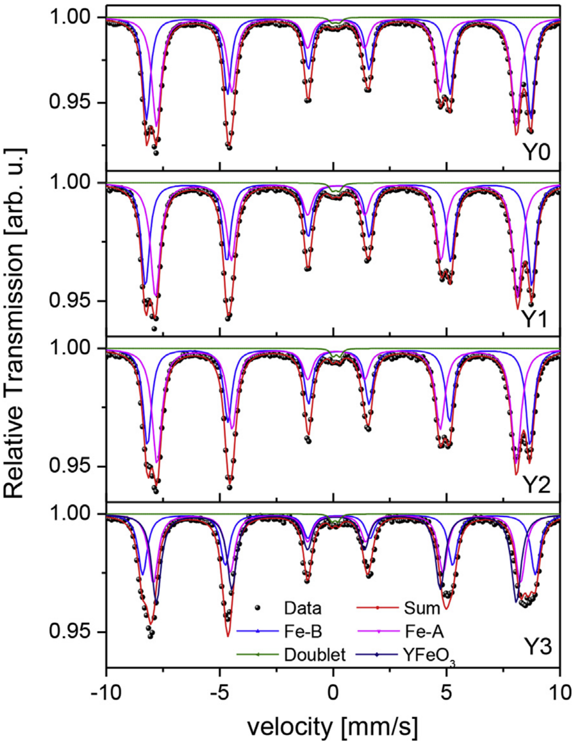

Fig. 3. Mössbauer spectra of Y0, Y1, Y2 and Y3 recorded at room temperature. Dots: experimental data; Solid lines: fitting curves. (Red: Sum spectrum; Blue: Fe-B sextet; Magenta: Fe-A sextet; Olive: SP doublet; Navy: $YFeO_3$ sextet (only in Y3)). (For interpretation of the references to colour in this figure legend, the reader is referred to the web version of this article.)

Table 3
Mössbauer spectra fitting data of the studied samples. Isomer shift (IS), hyperfine field (B_{hf}), area of each component (R_i) and Fe occupancy, F_i (i = A, B).

Sample	Component	IS [mm/s]	B_{hf} [T]	Area (R_i)	$F_i = n_{Fe}\, R_A/(R_B + R_A)$
Y0	Sextet (Fe-A)	0.24	49.1	41.1	0.827
	Sextet (Fe-B)	0.33	52.4	58.3	1.173
	Doublet (SP)	0.18	–	0.6	
Y1	Sextet (Fe-A)	0.24	49.4	38	0.687
	Sextet (Fe-B)	0.34	52.5	61.1	1.110
	Doublet (SP)	0.24	–	0.9	
Y2	Sextet (Fe-A)	0.23	48.7	43.5	0.754
	Sextet (Fe-B)	0.34	52.1	54.4	0.945
	Doublet (SP)	0.22	–	1.1	
Y3	Sextet (Fe-A)	0.23	49.0	46.2	0.795
	Sextet (Fe-B)	0.32	52.2	50.7	0.875
	Doublet (SP)	0.20	–	1.5	
	$YFeO_3$ (Sextet)	0.30	50.8	1.1	

growth. The similar tendency of the lattice parameter *a* and crystalline size D_{Sch} with Y content (Fig. 5) supports this hypothesis.

For Y0, both D_{Sch} and D_m show similar values, indicating single-crystal nanoparticles.

3.3. Raman analysis

Raman spectroscopy is a powerful tool for probing the lattice dynamics in several compounds. In particular, it is a valuable technique for characterizing spinels because it is sensitive to the cation distribution in the lattice sites [19,20].

As mentioned in the Introduction, doped cobalt ferrite belongs to the cubic space group Fd-3m (O^7_h). Group theory predicts five first-order Raman active modes for perfectly inverse spinel ferrites [21]: 1 A_{1g}+1 E_g+3 T_{2g} which are observed in the 100 to 800 cm^{-1} range. The modes above 600 cm^{-1} are related to the vibrations in tetrahedral sites (T-modes), while the modes below this frequency are ascribed to the motion of the octahedral sublattice (O-modes) [22,23]. For magnetite, which is an inverse spinel, the following description of the normal modes is accepted [24]: A_{1g} –symmetric stretch of oxygen along Fe–O bonds; E_g and $T_{2g}(3)$ –symmetric and asymmetric bends of O with respect to Fe, respectively; $T_{2g}(2)$ –asymmetric stretch of Fe and O; $T_{2g}(1)$ –translatory movement of the whole tetrahedron FeO_4.

Fig. 6 displays the Raman spectra obtained for all the samples, which were fitted using eight Lorentzians and a constant background. The five theory-predicted modes ($T_{2g}(3)$; E_g; $T_{2g}(2)$; $T_{2g}(1)$ and $A_{1g}(1)$) are depicted with dashed (blue) lines, while three different modes are marked with an asterisk and solid (red) lines. The modes assignations were made accordingly with reports by other authors [21,25,26] and are tabulated together with the peaks positions in Table 5.

The three new modes do not seem related to the inclusion of Y in the lattice, since they are also observed in Y0. However, Y content seems to play an important role in determining the relative intensities of the T-modes (the three bands above 600 cm^{-1}).

According to X-ray results, the samples are not perfectly inverse spinels and the inversion factor δ is affected by Y substitution, as shown in Table 2. The change in δ is related to a cation reordering between A and B sublattices, therefore reducing the symmetry of the lattice and modifying the allowed vibrations, which originates new first-order Raman modes at different frequencies [18]. As the lattice symmetry is reduced, new modes are to be expected [7,25,27]. Out of the three new modes observed, there is one ascribed to vibrations of the octahedral sublattice (O-mode, at ~365 cm^{-1}) and two T-modes (due to A_{1g} symmetry –$A_{1g}(2)$ and A_{1g} (3) in Table 5). Chandramohan et al., in their Raman study of $CoFe_2O_4$, also observe the rising of two bands at 625 cm^{-1} and 370 cm^{-1} (this last peak is noticed in their spectra, however the authors do not consider its contribution for the fitting of the profiles) [25]. We were not able to assign this peak to a normal mode, but infer that is not strongly dependent on Y substitution because its position and relative intensity are almost the same for the four samples. The new band assigned to an $A_{1g}(3)$ symmetry (at ~665 cm^{-1}) has not been reported for spinels by other authors.

Yttrium substitution seems to alter mainly the T-modes of the Raman spectra, and important differences in the relative intensity of the bands above 600 cm^{-1} are observed. In order to account for the presence of three T-modes and their change in relative intensity, we propose the following interpretation. As already determined by Rietveld refinements of the X ray diffractograms, tetrahedral sites are occupied by both Fe^{3+} and Co^{2+} ions, which produce three different kinds of bonds in A sites, namely Fe–*O*–Fe, Fe–*O*–Co and Co–*O*–Co. The vibration of each kind of bond is of A_{1g} symmetry, but at a different wave number, thus giving rise to the three observed T-modes. Kumar et al. [28] observe a blue shift in the vibrational modes of $CoFe_2O_4$ when half of the Co^{2+} ions are replaced by Ni^{2+}, with a lower atomic mass. Following this idea, and considering that Co has a higher atomic mass than Fe (58.9 g for Co and 55.8 g for Fe) it is possible to assign the highest wave number $A_{1g}(1)$ band (at ~700 cm^{-1}) to the vibration of Fe–*O*–Fe bonds, the lowest $A_{1g}(2)$ band (at ~630 cm^{-1}) to the vibration of the heaviest Co–*O*–Co bonds, and the third observed T-mode in between these two (the $A_{1g}(3)$ mode) to the Fe–*O*–Co bonds.

Given that the $T_{2g}(2)$ band seems the most unchanged with Y substitution, it was chosen to compare the relative intensities of the T-modes. The intensity ratios $I_{v1} = I(A_{1g}(1))/I(T_{2g}(2))$ related to vibrations of the Fe–*O*–Fe bonds and $I_{v2} = I(A_{1g}(2))/I(T_{2g}(2))$ related to Co–*O*–Co bonds were calculated and are shown in Fig. 7 a. A

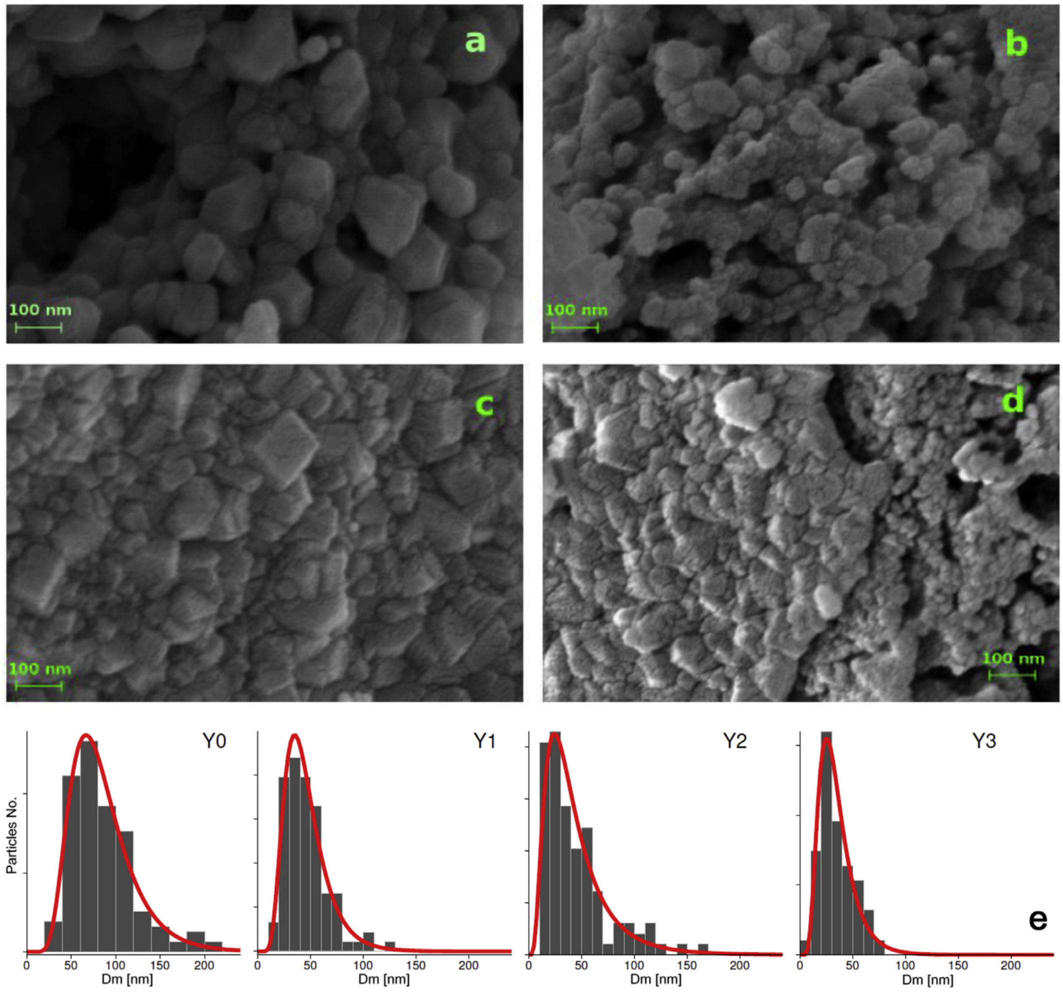

Fig. 4. SEM images of samples Y0 to Y3 (a to d, respectively) and particle size distributions (e).

Table 4
Crystallite size D_{Sch} from XRD results and mean particle size, from SEM images (D_m).

Sample	D_{Sch} [±5 nm]	D_m [±3 nm]
Y0	80	85
Y1	27	46
Y2	25	45
Y3	24	34

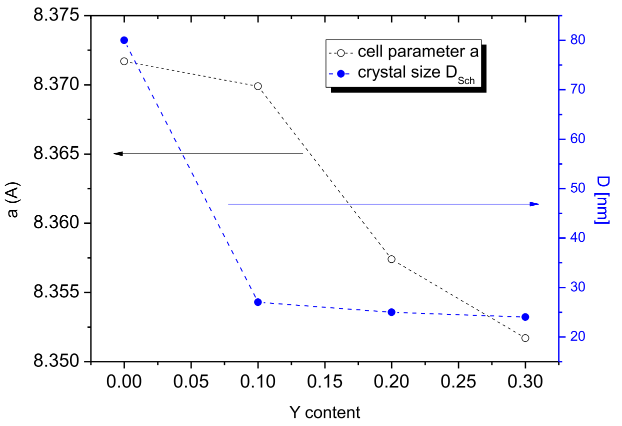

Fig. 5. Cell parameter *a* and crystallite sizes D_{Sch} as a function of Y content.

good correlation with this behavior is observed in Fig. 7 b, where the tetrahedral site occupancy by Fe and Co ions is shown, indicating that the presence of the three T-modes are directly related to the cation distribution and, therefore, to Y substitution.

3.4. Magnetic measurements

Fig. 8 shows the hysteresis loops for samples Y0, Y1, Y2 and Y3. Ferrimagnetic behavior can be observed for all the samples. As Co ferrite is a relatively hard magnetic material, the M vs H curves show remanence (Mr) and coercivity (Hc). Table 6 lists the magnetic parameters for all the samples. The value of maximum magnetization M_{max} corresponds to the sample magnetization at 14.5 kOe, while saturation magnetization Ms was calculated as the y-intercept of the law of approach to saturation $M = Ms + b/H$, being *b* a constant.

Both Ms and Mr decrease with the increase in Y^{3+} content. Since the net magnetic moment of the sample is the difference between the magnetic moment of sublattice B, M_B, and the one of sublattice A, M_A, this decrease can only be explained by considering that Y^{3+} cations (without magnetic moment, i.e. $\mu = 0$) replace Fe^{3+} cations ($\mu = 5\ \mu_B$) in the octahedral sublattice of the spinel. In this way, M_B decreases accordingly with the increase in Y^{3+} content.

The values of Bohr magnetons per formula unit μ_B were calculated using the cation distribution refined with the Rietveld method (Table 2) and are shown in Table 6. The percentual decrease

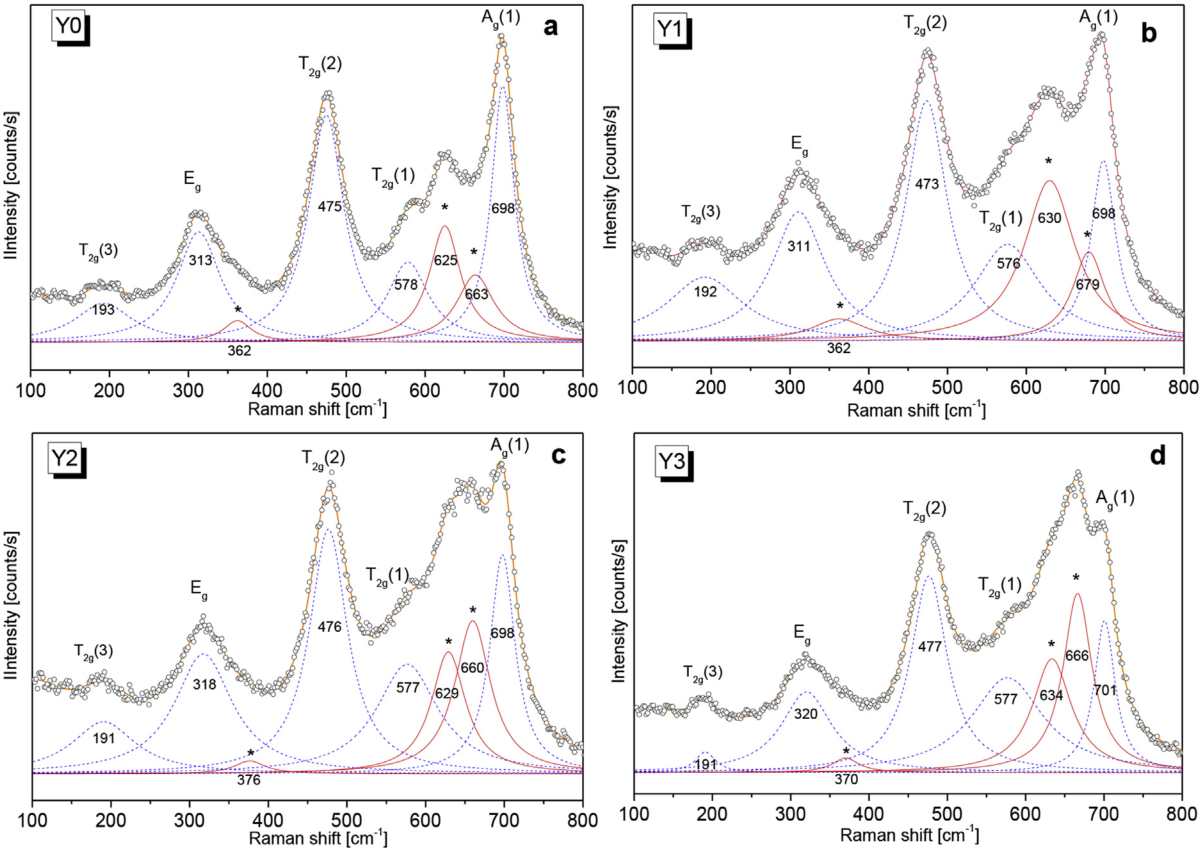

Fig. 6. Raman spectra for samples Y0 to Y3 (a to d, respectively). The dots correspond to the experimental data, dashed (blue) lines are the predicted modes for an inverse spinel and solid (red) lines marked with * are the new observed modes. Eight Lorentzians were used for the fit. (For interpretation of the references to colour in this figure legend, the reader is referred to the web version of this article.)

Table 5
Frequencies and assignation of the Raman modes for the studied samples.

Sample	Raman shift [cm^{-1}]							
	T_{2g} (3)	E_g	*	T_{2g} (2)	T_{2g} (1)	A_{1g} (2)*	A_{1g} (3)*	A_{1g} (1)
Y0	193	313	362	475	578	625	663	698
Y1	192	311	362	473	576	630	679	698
Y2	191	318	376	476	577	629	660	698
Y3	191	320	370	477	577	634	666	701

*: Not predicted by theory for inverse spinels.

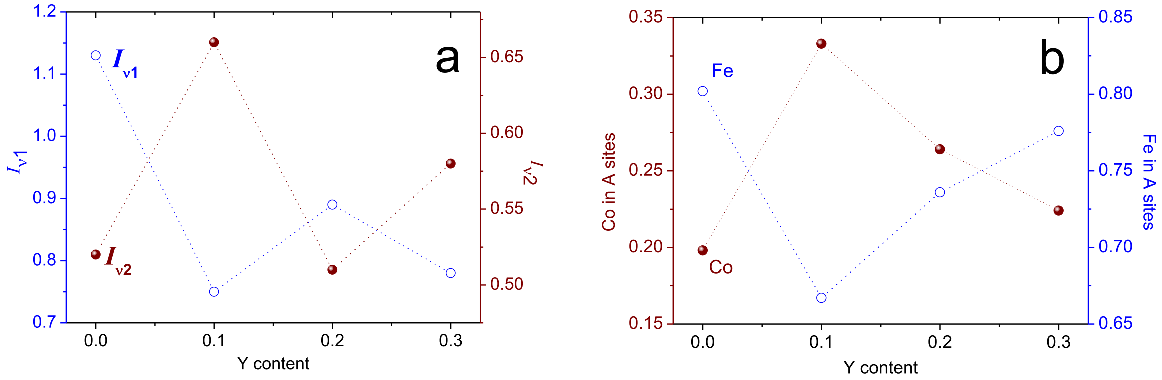

Fig. 7. Relative intensities I_{v1} and I_{v2} (a) and A-site occupancy of Fe and Co ions (b).

in μ_B with yttrium content agrees with the observed decrease in M_{max}, providing further support to the obtained cation distribution.

Coercivity increases in Y1 and Y2 with respect to Y0, and decreases for Y3. The increase in Hc is closely related with the particles size decrease and the increase in magnetocrystalline anisotropy associated with Y inclusion in the lattice. These characteristics have also been observed in similar systems [29].

The paramagnetic-to-ferromagnetic transition temperature (Curie temperature Tc) was obtained by measuring a TG (weight vs temperature) curve while applying a magnetic field to the sample. When the system undergoes the transition, a step-like feature is

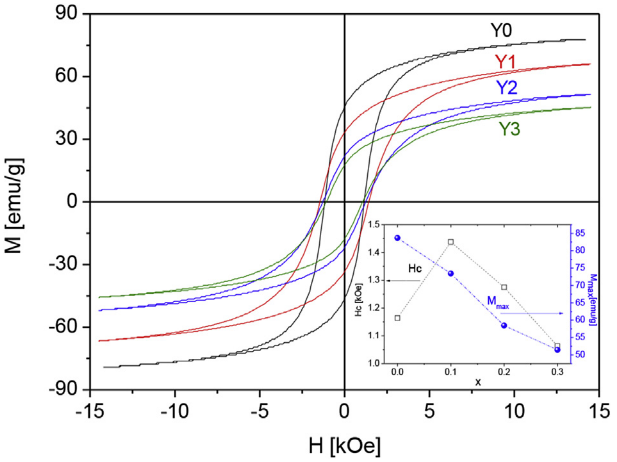

Fig. 8. Hysteresis loops of the studied samples. The inset shows the behavior of coercivity Hc (left axis) and maximum magnetization Mmax (right axis) as a function of Y content, x.

Table 6
Coercive field Hc, remanent magnetization Mr, saturation magnetization Ms and maximum magnetization at 14.5 kOe Mmax.

	Hc [±10 Oe]	Mr [±1 emu/g]	Mmax [±1 emu/g]	Ms [±2 emu/g]	μB
Y0	1165	46	76	84	3.8
Y1	1440	32	66	73	3.3
Y2	1275	22	50	58	2.6
Y3	1060	18	45	51	2.3

observed in the weight of the sample because the magnetic field has no longer the ability to attract the material. Tc was measured for all the samples, taking the maximum of the derivative d(weight)/dT (inset of Fig. 9). Fig. 9 shows that Tc decreases as a function of Y substitution from 444 °C in Y0 to 374 °C in Y3, owing to a decrease in the number of Fe–Fe superexchange interactions. Similar results on NiZn ferrite substituted with different rare earth ions were reported by Rezlescu et al. [30]. Because of the diamagnetic nature of Y^{3+}, its inclusion in B sites introduces a magnetic dilution in the A-B cation interaction, thus promoting a weakening in magnetic strength and therefore lower values for Tc.

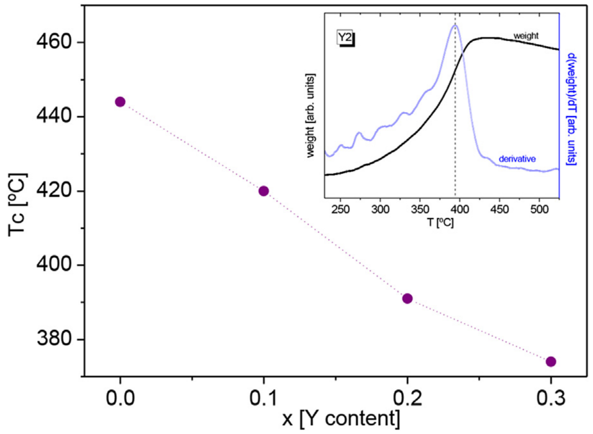

Fig. 9. Curie temperature Tc as a function of Y content. The inset shows the weight vs temperature curve for Y2 together with its derivative, which is representative of all the samples.

4. Conclusion

Cobalt ferrites of nominal composition $CoY_xFe_{1.98-x}O_4$, x = 0; 0.1; 0.2; 0.3, were prepared using the sol-gel combustion method. A slight iron deficiency in the formulation improved yttrium solubility in the spinel structure. Even when this strategy allowed to introduce an amount as high as 10% in the samples with lower yttrium content, a small amount of $YFeO_3$ was segregated (1.2 wt%) in the sample with x = 0.3, obtaining in this case an 8.5% cationic substitution.

A systematic decrease in cell parameters is observed with Y inclusion, despite the large size of Y^{3+}. According to X-ray results, the samples are not perfectly inverse spinels and the inversion factor δ is affected by Y substitution. The change in δ is related to cation reordering between A and B sublattices, which also modifies the allowed lattice vibrations and originates new first-order Raman modes as a result of a lattice symmetry reduction.

Both magnetization and Curie temperature decrease with the increase in Y^{3+} content due to cation distribution and owing to a decrease in the number of Fe–Fe super-exchange interactions in the octahedral sublattice.

Acknowledgments

This work was partially funded by Secyt-UNC and UBACyT. The authors wish to thank Dr. Víctor Galván for his valuable help with FullProf Suite and Rietveld refinements. The authors thank Dr. B. Arcondo for Mössbauer measurements (FIUBA).

References

[1] M.M. Rashad, D.A. Rayan, A.O. Turky, M.M. Hessien, Effect of Co^{2+} and Y^{3+} ions insertion on the microstructure development and magnetic properties of $Ni_{0.5}Zn_{0.5}Fe_2O_4$ powders synthesized using Co-precipitation method, J. Magn. Magn. Mater. 374 (2015) 359–366.

[2] J. Smit, H.P.J. Wijn, Ferrites, Philips Technical Library, 1959.

[3] D. Carta, M.F. Casula, A. Falqui, D. Loche, G. Mountjoy, C. Sangregorio, A. Corrias, A structural and magnetic investigation of the inversion degree in ferrite nanocrystals MFe_2O_4 (M = Mn, Co, Ni), J. Phys. Chem. 113 (20) (2009) 8606–8615, http://dx.doi.org/10.1021/jp901077c.

[4] G. Bulai, L. Diamandescu, I. Dimitru, S. Gurlui, M. Fede, O.F. Caltun, Effect of rear earth substitution in cobalt ferrite bulk materials, J. Magn. Magn. Mater. 390 (2015) 123–131.

[5] S. Kumari, V. Kumar, P. Kumar, M. Kar, L. Kumar, Structural and magnetic properties of nanocrystalline yttrium substituted cobalt ferrite synthesized by the citrate precursor technique, Adv. Powder Technol. 26 (2015) 213–223, http://dx.doi.org/10.1016/j.apt.2014.10.002.

[6] M.K. Shobana, Hoon Kwon, Heeman Choe, Structural studies on the yttrium-doped cobalt ferrite powders synthesized by sol-gel combustion method, J. Magn. Magn. Mater. 324 (2012) 2245–2248.

[7] X. Zhao, W. Wng, Y. Zhang, S. Wu, F. Li, J. Ping Liu, Synthesis and characterization of gadolinium doped cobalt ferrite nanoparticles with enhanced adsorption capability for Congo Red, Chem. Eng. J. 250 (2014) 164–174.

[8] X. Meng, H. Li, J. Chen, L. Mei, K. Wang, X. Li, Mössbauer study of cobalt ferrite nanocrystals substituted with rare-earth Y ions, J. Magn. Magn. Mater. 321 (2009) 1155–1158, http://dx.doi.org/10.1016/j.jmmm.2008.10.041.

[9] M. Ishaque, M. Azhar Khan, I. Ali, H.M. Khan, M. Asif Iqbal, M.U. Islam, M. Farooq Warsi, Study on the electromagnetic behavior evaluation of Y^{3+} doped cobalt nanocrystals synthesized via co-precipitation route, J. Magn. Magn. Mater. 372 (2014) 68–73.

[10] E. Ateia, M.A. Ahmed, A.K. El-Aziz, Effect of rare earth radius and concentration on the structural and transport properties of doped Mn–Zn ferrite, J. Magn. Magn. Mater. 311 (2007) 545–554.

[11] H. Mehmood Khan, Misbah-ul Islam, Irshad Ali, Mazhar-ud-din Rana, Electrical transport properties of Bi_2O_3-Doped $CoFe_2O_4$ and $CoHo_{0.02}Fe_{1.98}O_4$ ferrites, Mater. Sci. Appl. 2 (2011) 1083–1089.

[12] S.E. Jacobo, C. Herme, P.G. Bercoff, Influence of the iron content on the formation process of substituted Co-Nd strontium hexaferrite prepared by the citrate precursor method, J. Alloys Compd. 495 (2) (2010) 513–515, http://dx.doi.org/10.1016/j.jallcom.2009.10.172.

[13] C. Herme, S. Jacobo, P.G. Bercoff, B. Arcondo, Mössbauer analysis of Nd-Co M-type strontium hexaferrite powders with different iron content, Hyperfine Interact. 195 (1) (2010) 205–212.

[14] C.A. Herme, P.G. Bercoff, S.E. Jacobo, Nd-Co substituted strontium hexaferrite powders with enhanced coercivity, Mater. Res. Bull. 47 (2012) 3881–3887.

[15] E.E. Sileo, S.E. Jacobo, Gadolinium-Nickel ferrites prepared from metal citrates precursors, Phys. B 354 (2004) 241–245.
[16] R.Y. Young, The Rietveld Method, third ed., Oxford University Press, 1996.
[17] M. Ishaque, M. Azhar Khan, I. Alia, H.M. Khan, M. AsifIqbal, M.U. Islam, M. Farooq Warsi, Investigations on structural, electrical and dielectric properties of yttrium substituted Mg-ferrites, Ceram. Int. 41 (2015) 4028–4034.
[18] G.A. Sawatzky, F. Vander Woude, A.H. Morrish, Recoilless-fraction ratios for Fe57 in octahedral and tetrahedral sites of a spinel and a garnet, Phys. Rev. 183 (1969) 383.
[19] M. Lazzeri, P. Thibaudeau, Ab initio Raman spectrum of the normal and disordered $MgAl_2O_4$ spinel, Phys. Rev. B 74 (14) (2006) 140301.
[20] G.A. de Wijs, C.M. Fang, G. Kresse, G. de With, First-principles calculation of the phonon spectrum of $MgAl_2O_4$ spinel, Phys. Rev. B 65 (9) (2002) 094305.
[21] P. Graves, C. Johnston, J. Campaniello, Raman scattering in spinel structure ferrites, Mater. Res. Bull. 23 (1988) 1651–1660.
[22] Z. Wang, D. Schiferl, Y. Zhao, H.St. C. O'Neill, High pressure Raman spectroscopy of spinel-type ferrite $ZnFe_2O_4$, J. Phys. Chem. Solids 64 (2003) 2517–2523.
[23] Yuqiu Qu, Haibin Yang, Nan Yang, Yuzun Fan, Hongyang Zhu, Guangtian Zou, The effect of reaction temperature on the particle size, structure and magnetic properties of coprecipitated $CoFe_2O_4$ nanoparticles, Mater. Lett. 60 (2006) 3548–3552.
[24] J.L. Verble, Temperature-dependent light-scattering studies of the Verwey transition and electronic disorder in magnetite, Phys. Rev. B 9 (1974) 5236–5248.
[25] P. Chandramohan, M.P. Srinivasan, S. Velmurugan, S.V. Narasimhan, Cation distribution and particle size effect on Raman spectrum of $CoFe_2O_4$, J. Solid State Chem. 184 (2011) 89–96.
[26] O.N. Shebanova, P. Lazor, Raman spectroscopic study of magnetite (FeFe2O4): a new assignment for the vibrational spectrum, J. Solid State Chem. 174 (2003) 424–430.
[27] Z. Wang, P. Lazor, S.K. Saxena, G. Artioli, High-Pressure Raman spectroscopic study of spinel ($ZnCr_2O_4$), J. Solid State Chem. 165 (2002) 165–170.
[28] A. Kumar, M. Dar, P. Sharma, D. Varshney, Structural and Raman scattering study of Ni-doped CoFe2O4, Solid State Phys. (2014) 1148–1150.
[29] S.E. Jacobo, P.G. Bercoff, Structural and electromagnetic properties of yttrium-substituted Ni–Zn ferrites, Ceram. Int. 42 (2016) 7664–7668.
[30] N. Rezlescu, E. Rezlescu, Comparative study of the effects of rare earth ions in a high frequency Ni-Zn ferrite, J. de Physique IV Colloque 7 (C1) (1997) 225–226.